

## Multi-water-bag models of ion temperature gradient instability in cylindrical geometry

David Coulette and Nicolas Besse

Citation: *Phys. Plasmas* **20**, 052107 (2013); doi: 10.1063/1.4804272

View online: <http://dx.doi.org/10.1063/1.4804272>

View Table of Contents: <http://pop.aip.org/resource/1/PHPAEN/v20/i5>

Published by the AIP Publishing LLC.

### Additional information on Phys. Plasmas

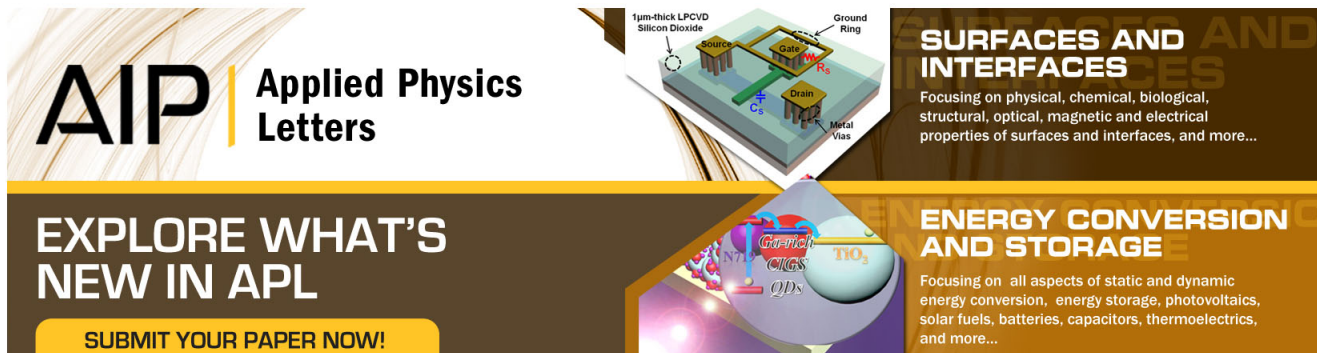
Journal Homepage: <http://pop.aip.org/>

Journal Information: [http://pop.aip.org/about/about\\_the\\_journal](http://pop.aip.org/about/about_the_journal)

Top downloads: [http://pop.aip.org/features/most\\_downloaded](http://pop.aip.org/features/most_downloaded)

Information for Authors: <http://pop.aip.org/authors>

## ADVERTISEMENT



**AIP | Applied Physics Letters**

**SURFACES AND INTERFACES**  
Focusing on physical, chemical, biological, structural, optical, magnetic and electrical properties of surfaces and interfaces, and more...

**ENERGY CONVERSION AND STORAGE**  
Focusing on all aspects of static and dynamic energy conversion, energy storage, photovoltaics, solar fuels, batteries, capacitors, thermoelectrics, and more...

**EXPLORE WHAT'S NEW IN APL**

**SUBMIT YOUR PAPER NOW!**

Labels in the schematic: 1µm-thick LPCVD Silicon Dioxide, Source, Gate, Drain, Metal Vias, Ground Ring, Cs, R<sub>s</sub>.

Labels in the energy conversion diagram: QDs, CIGS, NTG, NO<sub>2</sub>.

# Multi-water-bag models of ion temperature gradient instability in cylindrical geometry

David Coulette<sup>1,a)</sup> and Nicolas Besse<sup>2,b)</sup>

<sup>1</sup>*Institut Jean Lamour UMR CNRS 7198 Département Physique de la Matière et des Matériaux, Université de Lorraine, Faculté des Sciences et Technologie, Campus Victor Grignard BP 70239, 54506 Vandoeuvre-lès-Nancy Cedex, France*

<sup>2</sup>*Institut Jean Lamour UMR CNRS 7198 Département Physique de la Matière et des Matériaux and Institut Elie Cartan UMR CNRS 7502 INRIA Calvi Team, Université de Lorraine, Faculté des Sciences et Technologie, Campus Victor Grignard BP 70239, 54506 Vandoeuvre-lès-Nancy Cedex, France*

(Received 31 January 2013; accepted 19 April 2013; published online 8 May 2013)

Ion temperature gradient instabilities play a major role in the understanding of anomalous transport in core fusion plasmas. In the considered cylindrical geometry, ion dynamics is described using a drift-kinetic multi-water-bag model for the parallel velocity dependency of the ion distribution function. In a first stage, global linear stability analysis is performed. From the obtained normal modes, parametric dependencies of the main spectral characteristics of the instability are then examined. Comparison of the multi-water-bag results with a reference continuous Maxwellian case allows us to evaluate the effects of discrete parallel velocity sampling induced by the Multi-Water-Bag model. Differences between the global model and local models considered in previous works are discussed. Using results from linear, quasilinear, and nonlinear numerical simulations, an analysis of the first stage saturation dynamics of the instability is proposed, where the divergence between the three models is examined. © 2013 AIP Publishing LLC. [<http://dx.doi.org/10.1063/1.4804272>]

## I. INTRODUCTION

Ion temperature gradient (ITG) instabilities play a major role in the understanding of anomalous transport in core fusion plasmas. Considerable research efforts have been invested in the past decades in the study of the inherently complex dynamics of drift-waves/zonal flow driven turbulence,<sup>9,10,15</sup> either through fluid or gyrokinetic<sup>2</sup> models. Numerous high performance gyrokinetic simulation codes<sup>5,6,8,11</sup> have been developed to allow for the numerical study of the instability growth and saturation processes, as well as its impact on transport and require substantial amount of computing resources. In the following study, the analysis is restricted to cylindrical geometry, where magnetic field gradient and curvature effects are neglected, and the drift-kinetic limit ( $\mu \rightarrow 0$ ) of the gyrokinetic model for the description of ion dynamics. A specificity of our approach is the use of the so-called Multi-Water-Bag (MWB) model for the parallel velocity dependency of the ion guiding centers distribution function. This model was leveraged in the previous works<sup>7,12–14</sup> for the linear analysis of both collisional drift waves and ITG modes in cylindrical geometry. While differing both in the kind of instability studied or the selection of finite Larmor radius effects taken into account, those previous studies all considered a radially local treatment of the instability, either by using an ansatz for the radial envelope of the electrostatic potential normal modes<sup>7,12</sup> or neglecting polarization drift.<sup>13,14</sup> In this work, we consider a model where the radial differential eigenvalue problem

arising from the introduction of the polarization drift in the quasi-neutrality equation is solved in order to obtain both temporal (frequencies and growth rates) and geometric (radial envelopes) characteristics of the unstable normal modes. Comparing results obtained from the ansatz and radially solved models, we observed previously<sup>3</sup> a significant sensitivity of the ansatz method results to the choice of ansatz. A second difference arising from the radially solved method presented hereafter lies in the nature of equilibrium quantities. In both local and global models, the multi-water-bag parameters for low number of bags cases are obtained by a constraint on the parallel velocity moments of the distribution function. The extension of this moment constraint from a single radial position to the whole radial domain restricts the control on the sampling of the parallel velocity dimension brought for by the multi-water-bag model. For both aforementioned reasons, no point-to-point quantitative comparison can be made of our results with those previous works. Qualitative differences in overall parametric behavior will nonetheless be pointed out when deemed significant. In a first part, reduction of the problem dimension is obtained by using a multi-water-bag model for the parallel velocity dependency of the ion distribution function. Under hypotheses on turbulence and mean fields levels and evolution time scales, linear and quasilinear dynamical models are then obtained from the initial full nonlinear one. The second part is devoted to global linear stability analysis. Main characteristics of the unstable normal modes are examined, and comparison with a continuous Maxwellian model is used to evaluate the finite sampling effects of the Multi-Water-Bag reduction and the influence of the number of bags. This allows us to choose a bag number showing an acceptable

<sup>a)</sup>Electronic mail: david.coulette@ijl.nancy-universite.fr

<sup>b)</sup>Electronic mail: nicolas.besse@univ-lorraine.fr

compromise between accuracy and computing costs for the subsequent nonlinear study. In a third part, numerical simulation results of the instability growth and early saturation stages from the three dynamical models are analyzed and early saturation mechanisms discussed.

## II. MULTI-WATER-BAG MODEL IN THE DRIFT-KINETIC LIMIT

### A. Main physical model description

The physical system under consideration is a cylindrical plasma column of length  $L_z$  and radius  $a$ , magnetized by a constant axial magnetic field  $\mathbf{B}_0 = B_0 \mathbf{u}_z$ . The  $z$  direction is considered periodic, giving the cylinder toroidal topology. We consider a single population of ions of mass  $m_i$ , charge  $q_i = eZ_i$ , and vanishing magnetic moment  $\mu \approx 0$ , whose parallel velocity distribution function obeys the drift-kinetic evolution equation

$$\partial_t f + \mathbf{V}_{E \times B} \cdot \nabla_{\perp} f + v_z \partial_z f - \frac{q_i}{m_i} \partial_z \phi \partial_{v_z} f = 0, \quad (1)$$

where  $\mathbf{V}_{E \times B} = \mathbf{u}_z \times \nabla \phi / B_0$ ,  $\phi$  is the electrostatic potential. To describe the parallel ion dynamics, we define a MWB distribution function as a finite sum of constant height gate functions in  $v_z$ , the so-called ‘‘water-bags,’’ in the form

$$f(\mathbf{r}, v_z, t) = \sum_j A_j \mathcal{H}(v_j(\mathbf{r}, t) - v_z), \quad (2)$$

where  $\mathcal{H}$  is the Heaviside function,  $j$  ranges from  $-N$  to  $N$  excluding  $j=0$ ,  $A_j > 0$  for  $j = 1, \dots, N$  are the bags heights,  $A_{-j} = -A_j$ , and the couples  $(v_{-j}, v_j), j = 1, \dots, N$  define the bounds of the water-bag in  $v_z$  and bear the spatial and temporal dependency of the distribution. A distribution of the form (2) is an exact weak solution of Eq. (1) provided the contours  $v_j$  are smooth, do not cross and obey the transport equation

$$\partial_t v_j + \mathbf{V}_{E \times B} \cdot \nabla v_j + \partial_z \left[ \frac{q_i}{m_i} \phi + \frac{v_j^2}{2} \right] = 0. \quad (3)$$

The four-dimensional equation (1) is thus reduced to a system of three-dimensional fluid-like transport equations. Electrons are considered adiabatic with  $e\phi/k_B T_e \ll 1$ , and the system is closed by the linearized quasi-neutrality equation with polarization-drift

$$-\nabla \cdot \frac{Z_i n_{i0}}{B_0 \Omega_{CI}} \nabla_{\perp} \phi + \frac{n_{e0}}{k_B T_{e0}} (\phi - \langle \phi \rangle_{FS}) = Z_i n_i - n_{e0}, \quad (4)$$

where  $n_{i0}, n_{e0}, T_{e0}$  are given equilibrium radial profiles,  $\langle \cdot \rangle_{FS}$  denotes the flux surface average,  $n_i = \sum_j A_j v_j$  and the equilibrium electrostatic potential has been assumed vanishing so that  $Z_i n_{i0} = n_{e0}$ . Throughout the text, all quantities will be normalized using the following reference quantities defined from a reference on-grid radial position  $r_0 \approx a/2: \bar{T} = T_e(r_0)$ ,  $\bar{\tau} = \Omega_{CI}^{-1}$ ,  $\bar{v} = c_s = \sqrt{k_B T_e(r_0)/m_i}$ ,  $\bar{r} = \bar{z} = c_s/\omega_{CI}$ ,  $\bar{\phi} = k_B T_e(r_0)/q_i$ . Scalar fields  $X = v_j, \phi$  are decomposed along both periodic directions in Fourier series of the form  $X(r, \vartheta, z, t) = \sum X_m^n(r, t) \exp(im\vartheta + ink_{\parallel}z)$ , where  $k_{\parallel} = 2\pi/L_z$ .

### B. Dynamical approaches and corresponding codes

Without additional assumptions, systems (3) and (4) are solved by the semi-lagrangian Runge-Kutta code GMWB3d-SLCS.<sup>1</sup> It will be referred further on as the nonlinear model, as all nonlinearities in Eq. (3) are taken into account. Considering the  $(\vartheta, z)$  Fourier transform of Eq. (4) for a single mode  $(m, n)$ , under the hypothesis that the turbulence level is low, we neglect all coupling terms not involving the  $(0, 0)$  mode, leading to the transport equation

$$\partial_t v_{jm}^n + i(k_{\vartheta} \partial_r \phi_0^0 + nk_{\parallel} v_{j0}^0) v_{jm}^n + i(nk_{\parallel} - k_{\vartheta} \partial_r v_{j0}^0) \phi_m^n = 0. \quad (5)$$

The evolution of the  $(0, 0)$  mode is given by

$$\partial_t v_{j0}^0 + 2 \sum_{m,n>0} k_{\vartheta} \partial_r \Im(\phi_m^n v_{jm}^{n*}) = 0. \quad (6)$$

It must be emphasized that, contrary to Eq. (5), Eq. (6) does not rely on the small turbulence level hypothesis, and keeps the same form as in the non-linear model. Combining Eqs. (6), (5), and (4), one can obtain a self-consistent quasilinear model. We want, however, to be able to evaluate the impact of mode coupling truncation in Eq. (5) by comparing it to the nonlinear model, without the influence of the back reaction of the turbulence spectrum on the  $(0, 0)$  mode. We thus consider Eq. (5) driven by imposed  $(v_{j0}^0(r, t), \phi_0^0(r, t))$  fields whose time evolution is obtained from the nonlinear model data. This model will be further named the forced quasilinear model, keeping in mind that only half of the overall dynamics is solved. This model has been implemented in the initial value QUALIMUWABA code, using a simple 4th order Runge-Kutta scheme in time. Considering now that as some instant  $t_0$  the  $(0, 0)$  mode evolution is slow enough so that the driving terms of Eq. (5) can be considered as constant in time, we can solve the initial value problem for  $(v_{jm}^n(r, t), \phi_m^n(r, t))$  starting from time  $t_0$  using Fourier-Laplace transform. From Eq. (5) we obtain the coupling equation for an unstable mode  $(\tilde{v}_{jm}^n(r, \omega), \tilde{\phi}_m^n(r, \omega))$

$$\tilde{v}_{jm}^n = \frac{(nk_{\parallel} - k_{\vartheta} \partial_r v_{j0}^0) \tilde{\phi}_m^n + i v_{jm}^n(r, t = t_0)}{\omega - nk_{\parallel} v_{j0}^0 - k_{\vartheta} \partial_r \phi_0^0}, \quad (7)$$

where  $\omega = \omega_R + i\gamma$ ,  $\gamma > 0$ . By substituting Eq. (7) with vanishing initial condition into the quasi-neutrality equation, and defining  $\tilde{\psi}_m^n = \sqrt{rn_0} \tilde{\phi}_m^n$ , we obtain for the normal modes  $\tilde{\psi}_m^n$  the eigenvalue problem

$$[-d^2/dr^2 + Q_m^n(r, \omega)] \tilde{\psi}_m^n = 0, \quad (8)$$

with  $Q_m^n = B_m(r) + F_m^n(r, \omega)$  and

$$B_m(r) = k_{\vartheta}^2 + \frac{1}{Z_i T_e} + \frac{1}{\sqrt{rn_0}} \frac{d^2 \sqrt{rn_0}}{dr^2}, \quad (9)$$

$$F_m^n(r, \omega) = - \sum_j \frac{A_j}{n_0} \frac{nk_{\parallel} - k_{\vartheta} \partial_r v_{j0}^0}{\omega - nk_{\parallel} v_{j0}^0 - k_{\vartheta} \partial_r \phi_0^0}. \quad (10)$$

The eigenvalue problem defined by Eq. (8) with homogeneous Dirichlet boundary conditions at  $r_{min}$  and  $r_{max} = a$  is solved by the linear eigenvalue code CYLGYR.<sup>3</sup> For most results presented hereafter the nonlinear (with respect to the spectral parameter  $\omega$ ) eigenvalue solver of CYLGYR was used, as it is well suited when only the most unstable mode is sought for given spectral numbers  $(m, n)$ . The full  $\omega$ -linear solver, which allows to obtain the full spectrum and eigenvectors with a much higher computing cost, has been used for calibration and cross-checking tests with the nonlinear solver, and to ensure that the most unstable mode for given  $(m, n)$  can be considered as dominant, i.e., that the corresponding eigenvalue is well isolated. The code takes as input the  $(0, 0)$  mode contours and electrostatic potential profiles  $(v_{j0}^0(r, t), \phi_0^0(r, t))$ , either imposed for equilibrium studies or extracted from the nonlinear code data as in the forced quasilinear model. For each couple  $(m, n)$ , it provides an output frequency  $\omega_R = \Re\omega$ , growth rate  $\gamma = \Im\omega$ , and complex radial envelope  $\tilde{\phi}_m^n(r)$  of the most unstable mode. The validity of such a drastic selection in the spectrum relies on the assumption that this mode is effectively dominating the behavior at time  $t > t_0$ . To simplify notations, we will drop the  $(m, n)$  indexes in the following, as the comparisons will be made on eigenmodes for a given  $(m, n)$  couple. Let  $\tilde{\phi}_q$  be the right eigenvectors solutions of the eigenvalue problem at time  $t_0$  and  $\tilde{\chi}_q$  the corresponding left-eigenvectors. Let  $\tilde{\phi}_{q_{max}}$  be the complex envelope of the most unstable mode, with growth rate  $\gamma_{q_{max}}$ . The dominance condition writes

$$t - t_0 \gg \sup_{k \neq q_{max}} \left[ \frac{1}{\gamma_{q_{max}} - \gamma_k} \ln \left| \frac{\langle \tilde{\chi}_k | \tilde{\phi}(t_0) \rangle}{\langle \tilde{\chi}_{q_{max}} | \tilde{\phi}(t_0) \rangle} \right| \right], \quad (11)$$

where  $\langle u | v \rangle$  is the sesquilinear two-form used to define the adjoint problem. If  $(t - t_0)$  can be taken large enough, the most unstable mode will eventually be dominating even if the projection coefficient  $\langle \tilde{\chi}_{q_{max}} | \tilde{\phi}(t_0) \rangle$  of the initial state is not. Perturbing the equilibrium with a single eigenmode per  $(m, n)$  couple provides a quasi-perfect linear growth phase with a transient reduced to the minimum.<sup>3</sup> Considering now a discrete sequence of  $(0, 0)$ -mode profiles at times  $t_i$  and given  $(m, n)$ , the eigenbasis  $\tilde{\phi}_q(t_i)$  solution of the eigenproblem at time  $t_i$ , one can follow the evolution of the most unstable mode characteristics  $(\tilde{\phi}_{q_{max}}(t_i), \gamma_{q_{max}}(t_i), \omega_{q_{max}}(t_i))$ . We emphasize the fact that, even if the  $(0, 0)$  adiabaticity condition is fulfilled, those characteristics necessarily diverge with the equivalent ones computed on the real state, as the projection of an eigenmode at time  $t_i$  spans several eigenmodes in the basis computed at time  $t_{i+1}$ . Taking instants  $t_i$  sufficiently short allows to reduce this spectral spreading (i.e., minimize the angle between  $\tilde{\phi}_{q_{max}}(t_i)$  and  $\tilde{\phi}_{q_{max}}(t_{i+1})$ ) but shortens the time necessary for mode dominance. With a proper adiabatic evolution, one could choose large enough time intervals with low spectral spreading thanks to the slow evolution of the eigenbasis. As will be shown later, this is not the case in the first saturation phase of the instability, leading to divergence between the adiabatic linear model and the forced quasilinear and nonlinear ones.

## C. Test cases description

### 1. Equilibrium parameters

All studies presented hereafter are based on three reference cases differing in radial size  $a = 9\rho_s$ ,  $a = 14.5\rho_s$ ,  $a = 20\rho_s$ . The limited range of radius chosen was no meant to provide  $\rho^* = \rho_s/a$  scan studies, but to allow variations in unstable zone width and position keeping constant radial sample number. Equilibrium density and temperature radial profiles are staircase-shaped ones defined by  $X(r) = \exp\left(\kappa_X \Delta_{r_X} \tanh\left(\frac{r-r_X}{\Delta_{r_X}}\right)\right)$  with  $X \in \{n, T\}$ , leading to radially localized  $\eta_i$  profiles (Fig. 1). In all cases considered here,  $Z_i = 1$  and  $T_e = T_i$ . The three reference parameters sets are given in Table I. All parametric studies are done by varying one or a few parameters, domain size excepted, from this three cases. In all cases, the equilibrium electrostatic field is assumed nonexistent. The equilibrium multi-water-bag parameters are obtained by imposing that the  $N$  first even parallel velocity moments of the MWB distribution equate those of a Maxwellian. Using a homotopy continuation procedure,<sup>3</sup> this condition is fulfilled up to machine precision on the whole radial domain.

### 2. Simulation scenarii

In a first linear analysis stage, the normal modes corresponding to the equilibrium are computed. A perturbed state is built by adding to the equilibrium fields perturbations of the form

$$\tilde{X} = \epsilon_{glob} \sum_{q=1}^p \epsilon_q \tilde{X}_q(r) \cos(m_q \vartheta + n_q k_{\parallel} z + \alpha_q(r) + \beta_q), \quad (12)$$

where  $X \in \{v_j, \phi\}$ ,  $\epsilon_{glob}$  sets the perturbation level,  $\epsilon_q \in [0, 1]$  allow to weight the various normal modes,  $(X_q, \alpha_q)$  are the modulus and phase profiles of the  $q$ th normalized eigenmode of spectral parameters  $(m_q, n_q)$ ,  $\beta_q$  is a random constant phase factor. Numerical experiments were conducted using 1-mode, 2-modes, and many-modes (10 to 300) perturbations, where only the most unstable mode for each  $(m, n)$  couple was selected. The second phase consists in computing the time evolution of the system using the nonlinear code. In a third phase, the  $(z, \vartheta)$  averaged fields evolutions are extracted from the nonlinear code data and fed back to the forced quasilinear and linear codes.

## III. LINEAR ANALYSIS

In this section, a description of the main characteristics of the spectrum and eigenmodes of problem (8) is given. The influence of the multi-water-bag model is then examined by comparing its spectral characteristics with those of a ‘‘continuous’’ Maxwellian one.

### A. Spectrum and normal modes characteristics

For given  $(m, n)$  wavenumbers, the point spectrum obtained by solving the discretized problem (8) contains a large majority of real eigenvalues, leading to stable modes,

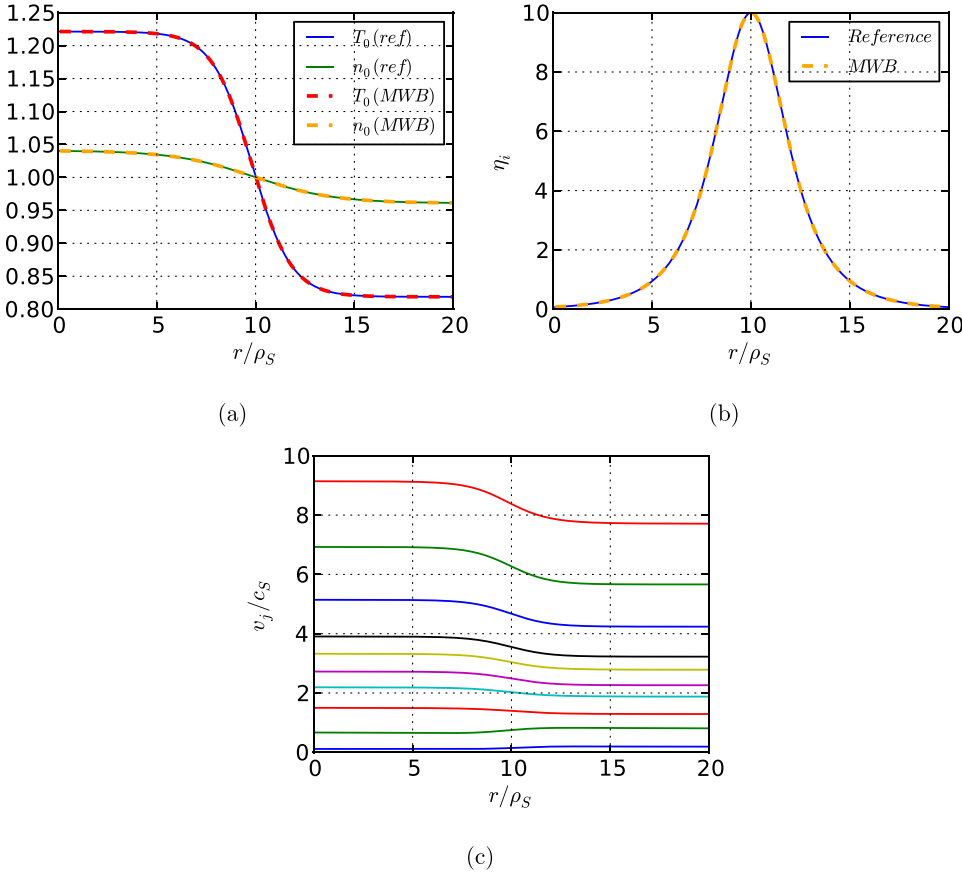


FIG. 1. Equilibrium radial profiles; density and temperature (a);  $\eta_i$  (b); MWB contours  $v_j(r)$  (c).

and a few unstable eigenmodes, representing at most 2% of the spectrum in the more favorable (large unstable zone) cases. The spectrum convex hull is also highly asymmetric, with  $\max|\omega_R| \propto 10^2 \max|\gamma|$ . Both characteristics make analysis near marginal stability difficult, as the conditioning of the eigenvalues near the real axis degrades. Moreover, the physical interpretation of eigenmodes for which  $\gamma \ll \gamma_{max}$  as unstable is dubious: in the case of an initial globally unstable equilibrium, they are quickly dominated by the more unstable modes, and in the case of a marginally stable state, with all modes either stable or nearly stable, they will be practically indistinguishable from stable modes. In all the following, all modes for which  $\gamma/(nk_{\parallel}) < 10^{-2}$  are considered as stable.

Considering only the most unstable mode for each spectral couple  $(m, n)$ , one can recover for a given equilibrium

the instability zone in the  $(m, n)$  spectral plane. This zone shows steep cutoffs in parallel wave number  $n$ . The low poloidal wave number  $m$  cutoff is also steep, with a slow nearly linear decrease for high  $m$  values (Fig. 2): this absence of clear cutoff is due to the fact that the only finite Larmor radius effect taken into account is the polarization drift, allowing small scales perturbations to develop. Frequency  $\omega_R$  exhibits an overall linear dependency on  $n$  with  $-\omega_R/(nk_{\parallel})$  of the order of unity (Fig. 3).

Mode envelopes are strongly localized in the  $\eta_i$  peaking radial region (Fig. 4), with low dispersion in the spectral plane  $(m, n)$  (Fig. 5(a)). Radial envelope characteristic width, estimated by computing the radial standard deviation  $\sigma$  of the envelope modulus and peak curvature (through

TABLE I. Reference cases parameters set.

Case name	SMALL	MEDIUM	BIG
$r_{min}/\rho_s$	1	0.1	0.1
$r_{max}/\rho_s$	9	14.5	20
$N_r$	128	128	128
Index $r_0$	64	64	64
$\kappa_n \rho_s$	$10^{-2}$	$5.51 \times 10^{-2}$	$10^{-2}$
$\Delta_{r_n}/\rho_s$	2	2.9	4
$\kappa_T \rho_s$	$10^{-1}$	$2.7586 \times 10^{-1}$	$10^{-1}$
$\Delta_{r_T}/\rho_s$	0.3	1.45	2
$k_{\parallel} \rho_s$	$10^{-3}$	$4.17 \times 10^{-3}$	$10^{-3}$
$N_{bag}$	6	6	6

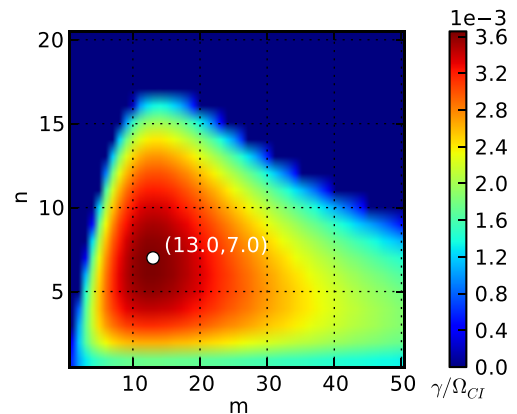


FIG. 2. Growth rate of the most unstable mode in the  $(m, n)$  spectral plane for the case BIG with  $N_{bag} = 10$ .

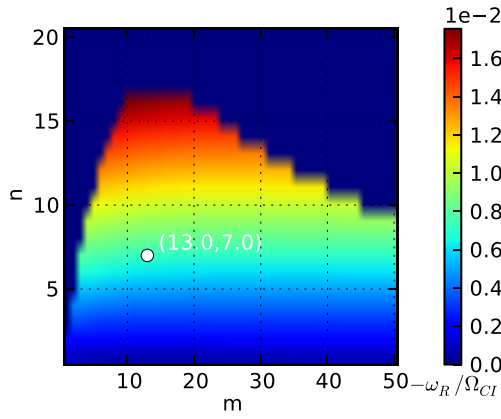


FIG. 3. Frequency of the most unstable mode in the  $(m, n)$  spectral plane for the case BIG with  $N_{bag} = 10$ .

$d_r^2 |\phi|(r_{peak})$ , is a decreasing function of  $k_{\vartheta}(r_{peak})$  for fixed  $n$  (Fig. 5(b)). In the considered cases and for fixed  $n$ , a parabolic model  $c_0 + c_1 k_{\vartheta} + c_2 k_{\vartheta}^2$  for the inverse width  $1/\sigma$  shows a good fit with the computed data. While this dependency is consistent with the direct parametric dependency of Eq. (8) in  $k_{\vartheta}$  if one neglects the  $m$  dependency of  $\omega$ , it is not guaranteed to be generalized as we have considered here only a specific class of strongly localized equilibrium gradient profiles. Radial phase variations (Fig. 4(b)) can reach significant values but do not cause a strong perturbation of overall mode geometry as they occur either in regions where envelope modulus is negligible or modulus variation is dominant. In order to examine more closely the correlation between the localization of the instability and the peaking gradient region, the latter is translated over the radial domain by varying the reference position  $r_0$ . Let us first consider the evolution during this scan of the characteristics of the most unstable mode over the whole  $(m, n)$  plane. The growth rate  $\gamma$  and normalized frequency  $X = \omega_R/(nk_{\parallel})$  of this mode are close to invariant by translation of the gradient zone. The radial position of this mode follows the peaking  $\eta_i$  one, and the poloidal wave number  $m$  evolves so as to maintain  $k_{\vartheta}(r_0)$  constant. This is confirmed more generally by observing the characteristics  $f(n, m) = \gamma(n, k_{\vartheta}(r_0))$ . For a fixed value of the parallel wave number  $n$ , the various curves  $f(n, m)$  nearly overlap, i.e.,  $f(n, m) \approx f(n)$  (Fig. 6).

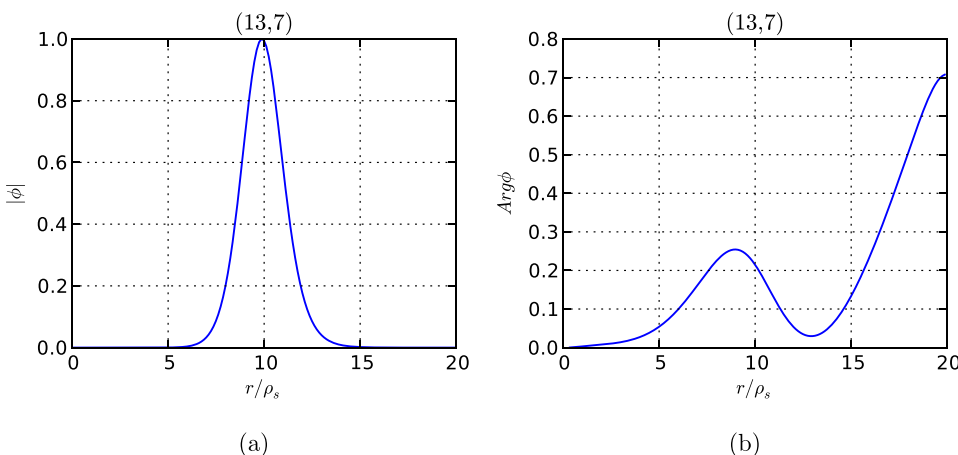


FIG. 4. Radial envelope of normal mode (13, 7) for the BIG case with  $N_{bag} = 10$ ; modulus (a); phase (b).

In all the previous results, only fairly localized unstable zones have been considered. Let us now consider a situation where the equilibrium  $\eta_i$  profile presents two peaking zones, i.e., when the density and temperature radial profiles exhibit two gradient steps (Fig. 7). The spectrum is first computed first for a unique  $\eta_i$ -peak located at  $r_1 = 5\rho_s$  (Fig. 8(a)), then for a unique  $\eta_i$ -peak located at  $r_1 = 15\rho_s$  (Fig. 8(b)), and finally for an equilibrium combining both  $\eta_i$  peaks. Interaction between the two unstable zones is evaluated by comparing the growth rates of the double  $\eta_i$ -peak equilibrium with the maximum of the growth-rates of the one-peak equilibria (Fig. 9), and checking the position and characteristics width of the mode envelope (Fig. 10). Combination of the two gradient zones has a slight destabilizing effect, leading to a widening of the unstable zone in the spectral plane. This coupling effect is weak in this situation, and the double-peak growth-rate map is very close to the maximum of the isolated peaks growth rates maps, confirming the essentially local nature of the instability.

## B. Model comparisons

Though the multi-water-bag distribution is an exact, albeit weak, solution of the Vlasov equation, the finite (and in our case small) number of bags induces a finite sampling in parallel velocity at each instant at a given position. To evaluate the effects on the obtained spectra and normal modes, the multi-water-bag model is compared with a continuous Maxwellian one (labeled as “kin” for “kinetic” in figures). Following the same perturbative treatment, one obtains the same eigenvalue problem on the Liouville transformed electrostatic potential  $\tilde{\psi}_m^n$  as Eq. (8), the only difference appearing in the density response function  $F_m^n(r, \omega)$  which takes the form

$$F_m^n = \frac{1}{T} \left( 1 + \xi Z \right) - \frac{k_{\vartheta}}{nk_{\parallel} \sqrt{2T}} \left( \left[ \kappa_n - \frac{\kappa_T}{2} \right] Z + \kappa_T \xi (1 + \xi Z) \right), \quad (13)$$

where  $\kappa_n = d_r \log n$ ,  $\kappa_T = d_r \log T$ ,  $\xi = \frac{\omega}{nk_{\parallel} \sqrt{T}}$ ,  $Z = Z(\xi)$  is the Fried and Conte function.<sup>4</sup> In this context, for a given radial position, the multi-water-bag form (10) can be viewed as a particular quadrature formula for Eq. (13), with  $2N$  quadrature points in parallel velocity. It should be noted that

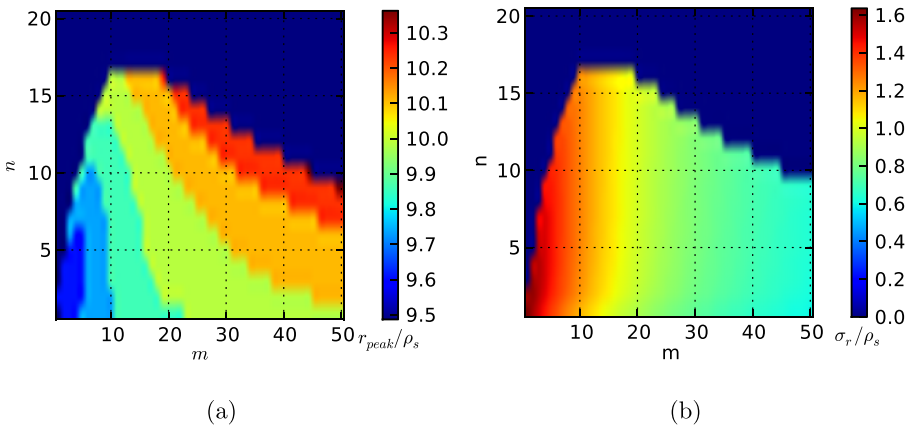


FIG. 5. Position  $r_{peak}$  and width  $\sigma$  of mode envelope modulus in the spectral plane.

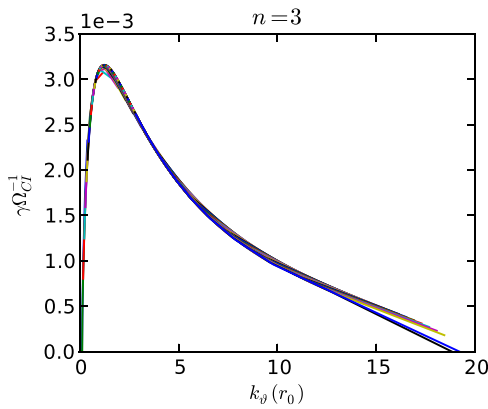


FIG. 6. BIG case; parametric scan of  $n_i$  peak position  $r_0$ ; overlap of growth-rates as function of  $k_{\parallel}(r_0)$  for modes  $(m, 3)$ ,  $m \in [1, 50]$ .

the numerical implementation of the continuous Maxwellian model cannot be strictly considered as continuous, as the computation of the Fried and Conte function relies on quadrature formulas as well; the “continuous” denomination relies on the high accuracy of those numerical quadratures. For small number of bags MWB distributions, i.e., small number of sampling points in  $v_{\parallel}$ , the number and position of  $v_{\parallel}$  sampling points may thus have a significant influence on the obtained spectrum. A first comparison is done for a given equilibrium, and performing a scan on the number of bags. For  $N_{bag} \geq 5$ , multi-water-bag growth rates and frequencies are in very good agreement for the low parallel wave number

part (small  $n$  values) of the spectrum (Fig. 11(a)), while discrepancies appear near the high parallel wave number cutoff (Fig. 11(b)). The higher sensitivity of the results on contour distribution for the larger  $n$  values can be explained by considering the ion density response function  $F_m^n(r, \omega)$  defined by Eq. (10), for a given radial position, as a function of the normalized frequency  $X = \omega_R / (nk_{\parallel}c_s)$ . The normalized growth rate  $Y$  acts as a damping factor which controls the broadness of the resonances at the poles defined by the contours  $v_j(r)$ . For small  $n$  values (Fig. 11(a)),  $Y$  is large enough compared to typical inter contour distance, to make the global response largely insensitive to individual contour position. For larger  $n$ , though (Fig. 11)  $Y$  decreases, the global response becomes sensitive to contour distribution. The absence of net convergence with the number of bags towards the continuous model in that case is due to the fact that the typical sampling density in parallel velocity does not vary significantly for the range of bag number scanned. Mode envelope geometry is well preserved, with negligible impact on modulus, and slight variation in phase (Fig. 12).

A second characterization of the influence of the number of bags is done by evaluating the gradient threshold of the instability. It should be noted that, as the eigenvalue problem is solved globally on the radial domain, the obtained spectrum is strictly speaking a functional of equilibrium radial profiles, all other parameters being kept constant. The infinite dimension space of equilibrium radial profiles does not allow to define a general stability criterion depending on a finite set of input parameters. Stability analysis is here

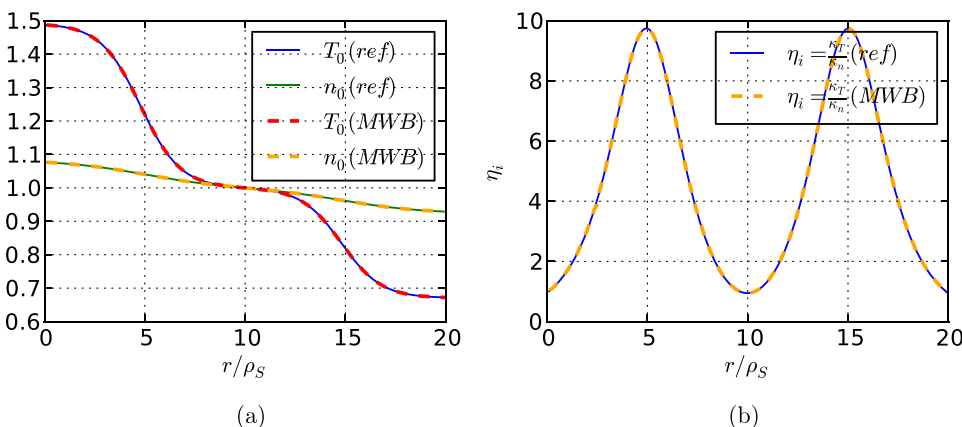


FIG. 7. Case BIG; double steps radial profiles; density and temperature (a);  $\eta_i$  (b).

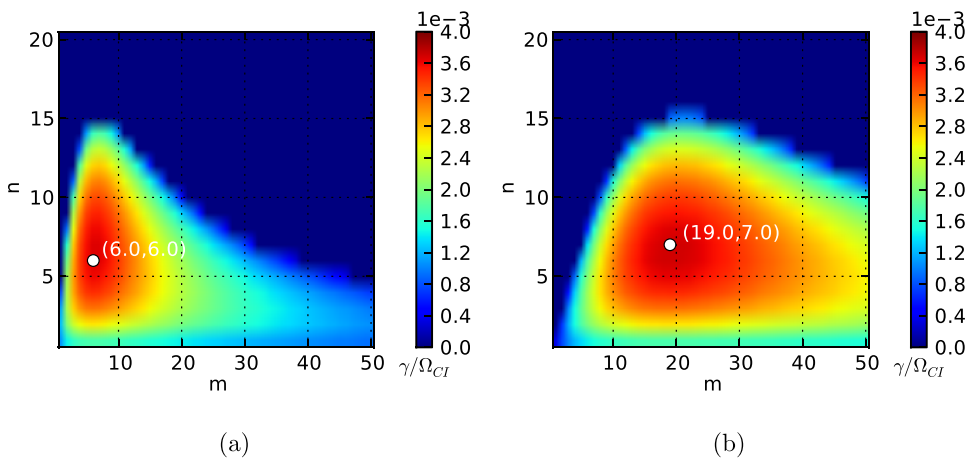


FIG. 8. Double  $\eta_i$  peak study; growth rates maps for each isolated peak equilibrium.

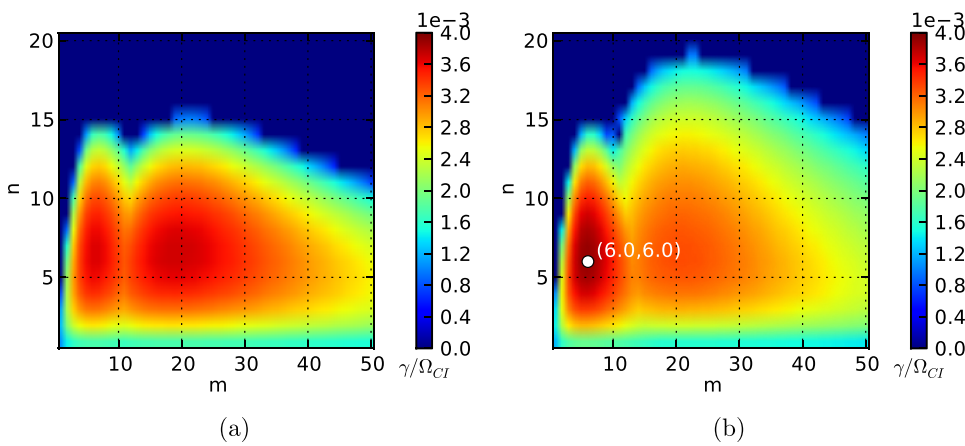


FIG. 9. Double  $\eta_i$ -peaks study; maximum of the isolated growth rates maps (a) and double peak growth rates map (b).

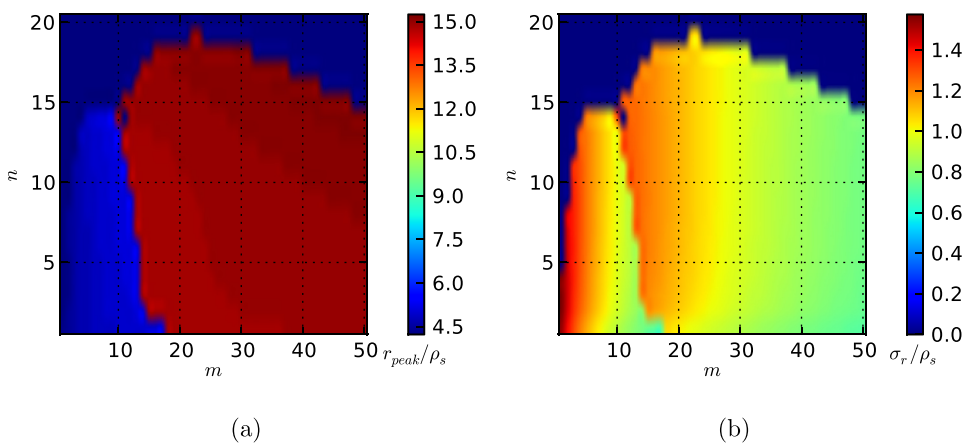


FIG. 10. Double  $\eta_i$  peak study; radial localization of the modes (a); characteristic mode width  $\sigma$  (b).

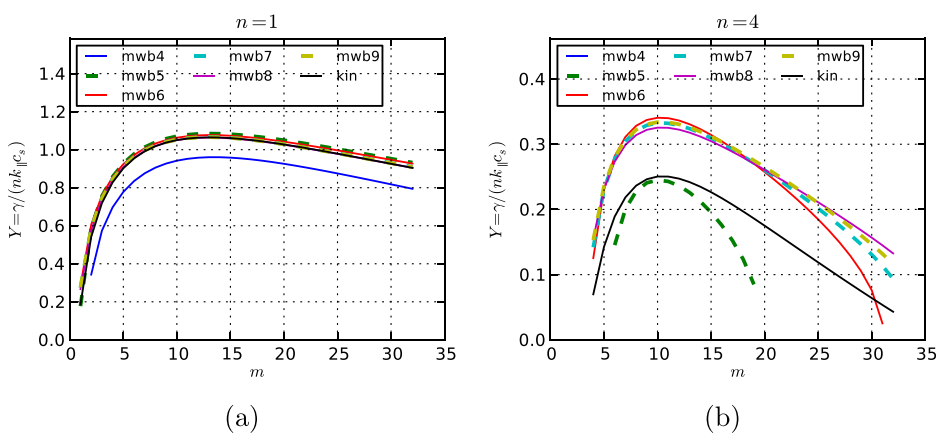


FIG. 11. SMALL case; normalized growth rates  $Y = \gamma/(nk_{\parallel}c_s)$  for the multi-water-bag model (mwbN) and continuous Maxwellian model (kin);  $n = 1$  (a),  $n = 4$  (b).

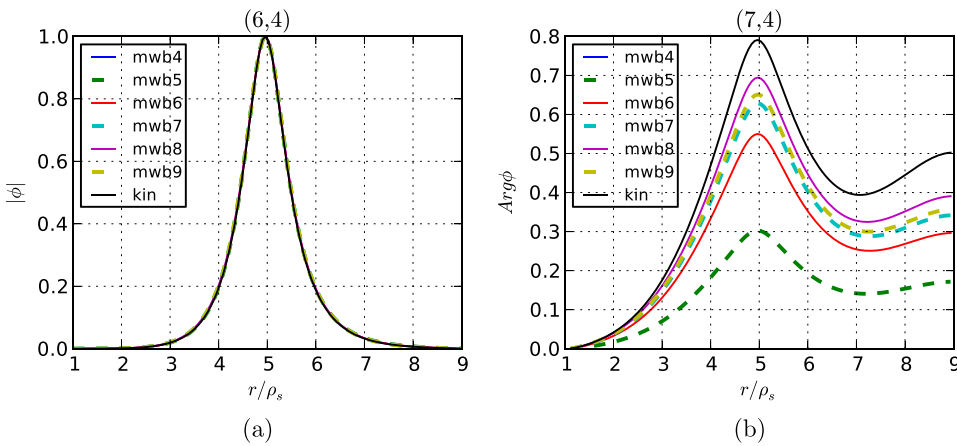


FIG. 12. SMALL case; model comparison of mode envelope geometry; modulus (a); phase (b).

restricted to a small subset of possible input equilibrium profiles: considering single gradient peak zone profiles localized at the center  $r_0$  of the radial domain, and keeping all other parameters constant, a scan in the peak density and temperature normalized gradients ( $\kappa_n(r_0), \kappa_T(r_0)$ ) is performed, and for each corresponding equilibrium, the maximum growth-rate over the whole  $(m, n)$  map is kept. Consistently with the previous observation, in the lower range of bag number scanned (5–8), the multi-water-bag instability threshold can differ significantly from the continuous one (Fig. 13(a)). The 10-bags distribution shows a good match with the continuous one. For this range of number of bags, there is no monotonic convergence with bag number to the continuous case, as the position of the bag contours has a non-negligible impact on the obtained thresholds. However, even in the case of the 6-bags MWB distribution, large discrepancies with the continuous Maxwellian model occur only for near-threshold values: for most of the scanned equilibria, relative errors on the growth-rate are below 10% (Fig. 13(b)).

A noticeable qualitative difference can be observed between the gradient scan results presented here and those obtained previously from a local model.<sup>14</sup> The multi-lobe structure of the stability zone boundary observed in the local model is replaced by a far smoother one in the non-local one.

### C. Concluding remarks

The multi-water-bag linear model allows, in the range of bag numbers considered, to describe with overall good

accuracy the features of the ITG instability. As for any discretization procedure with few sample points, the smallest bag number distributions ( $N=4, 5, 6$ ) may show sampling artifacts: the highest parallel wave numbers modes are less accurately described and their thresholds overestimated. For the following nonlinear simulations, 6-bags distributions were chosen, as an acceptable tradeoff between accuracy and computing costs.

## IV. SATURATION DYNAMICS OF THE INSTABILITY

Following the simulation work-flow described in Sec. II C 2, few-mode and many-modes perturbations simulations were conducted. Cross-validation of the three dynamical models in the linear growth phase of the instability was examined in a previous work:<sup>3</sup> growth rates, frequencies, and mode radial envelopes of the modes show good agreement, with relative variations of the order of 1%, establishing the consistency of the three models in this phase.

### A. Overview of relaxation dynamics

The overall behavior is the same in all considered situations: growth of the perturbation generates through nonlinearities both large scale modes, dominated by the  $(0, 0)$  one, and small scales ones. In all cases, the system relaxes towards marginal stability, with a broad low-level turbulence spectrum. It should be emphasized that, as Dirichlet boundary conditions are used for the  $(0, 0)$  electrostatic potential, longtime evolution of the system leads to dramatic increase

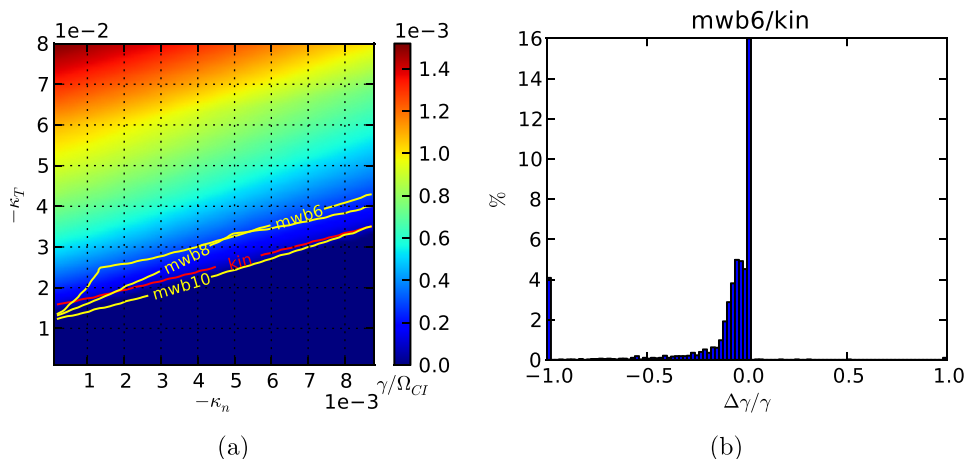


FIG. 13. SMALL case; model comparison; gradients scan over 2400 equilibria ( $30 \times 80$ ); maximum growth rate ( $\kappa_n, \kappa_T$ ) map for the continuous Maxwellian model and interpolated instability threshold lines for the multi-water-bags models (mwbN) and continuous Maxwellian (kin) (a); distribution of relative errors on growth-rates between the 6-bags MWB model and the continuous Maxwellian model (b).

of the mean radial electric field. No analysis of the time asymptotic state of the system can thus be conducted in that context, restricting the discussion to the initial relaxation stages. It is important to notice that the simulations scenarios considered here describe an overall free relaxation process. As a consequence, evolution of the (0, 0) mode entails congruent mean gradients relaxation and zonal flow generation. Comparing the mean density and temperature radial profiles between the initial and post-relaxation states, one observe an overall flattening of the temperature profile and steepening of the guiding-center density profile in the initial peaking gradient zone (Figs. 14 and 15). It should be noted that the latter does not entail any actual turbulent particle radial transport, but shows the difference between particles and guiding-centers density arising from the zonal flows through

the polarization drift. Dynamics of the relaxation of the (0, 0) mode and spectral evolution depend on the spectral broadness of the initial perturbation. For few-modes perturbations, mean gradients relaxation occurs in multiple stages (Fig. 16(a)), as the system goes through successive marginally stable and unstable states in regard to the initial perturbation (Fig. 17(a)), and a non-monotonic evolution towards global marginal stability (Fig. 17(b)). Zonal flow geometry (Fig. 18(a)), invariant in the linear phase, is strongly perturbed during the successive relaxation steps. For broad spectrum perturbations, this oscillatory behaviour is far less pronounced (Fig. 16(b)), with a quasi direct relaxation towards global marginal stability (Fig. 17(c)). Zonal flow geometry evolution shows as well a smoother transition from the linear phase envelope to the post-saturation one (Fig. 18(b)).

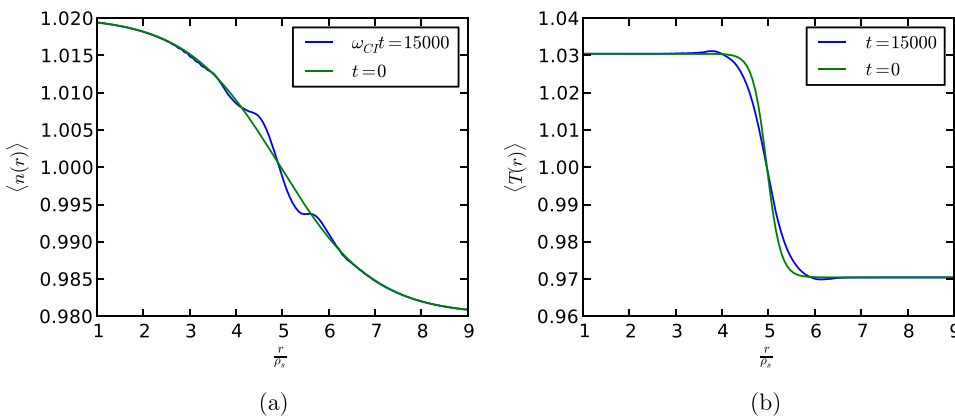


FIG. 14. SMALL case perturbed by (10, 5); mean density (a) and temperature (b) radial profiles at beginning and end of nonlinear simulation.

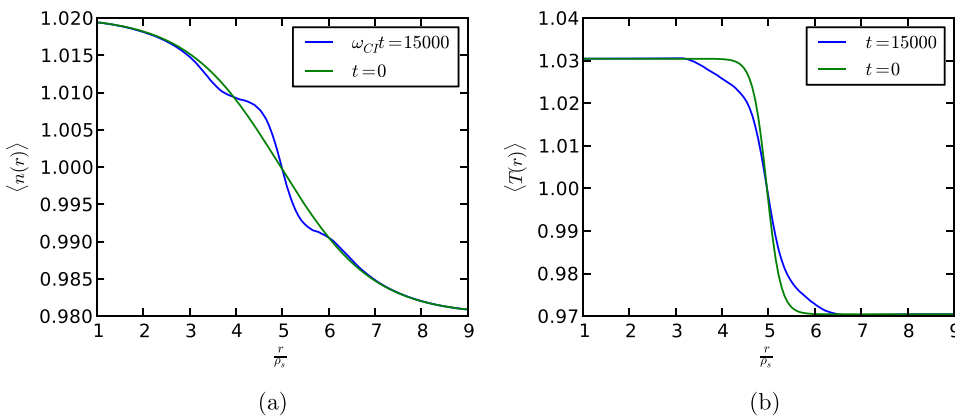


FIG. 15. SMALL case perturbed by 239 modes; mean density (a) and temperature (b) radial profiles at beginning and end of simulation.

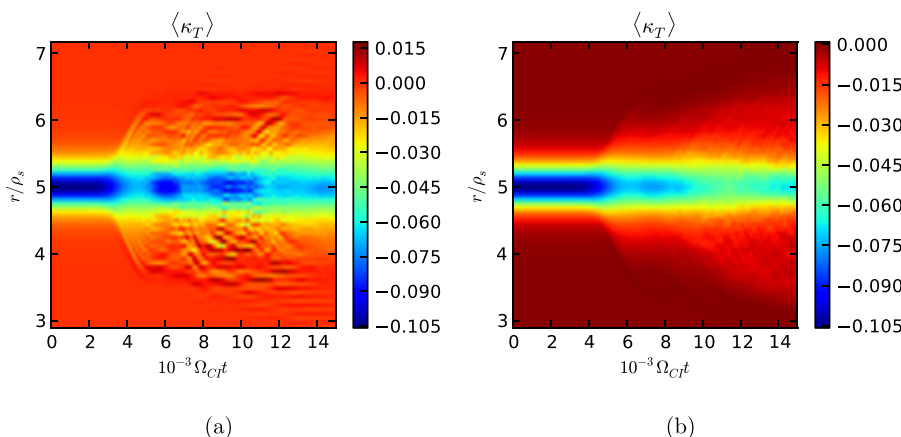


FIG. 16. SMALL case; time evolution of the mean normalized temperature gradient for single mode perturbation by (10, 5) (a) and 239 modes perturbation (b).

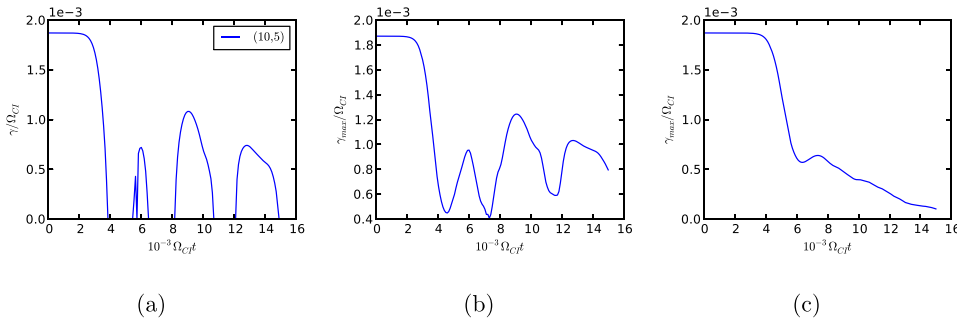


FIG. 17. SMALL case; linear growth rate evolution obtained from the linear code with (0, 0) mode fields extracted from nonlinear simulation data; growth rate of the (10, 5) mode for single mode perturbation by (10, 5) (a); maximum growth rate over (m, n) for the single mode perturbation by (10, 5) (b) and the 239 modes perturbation (c).

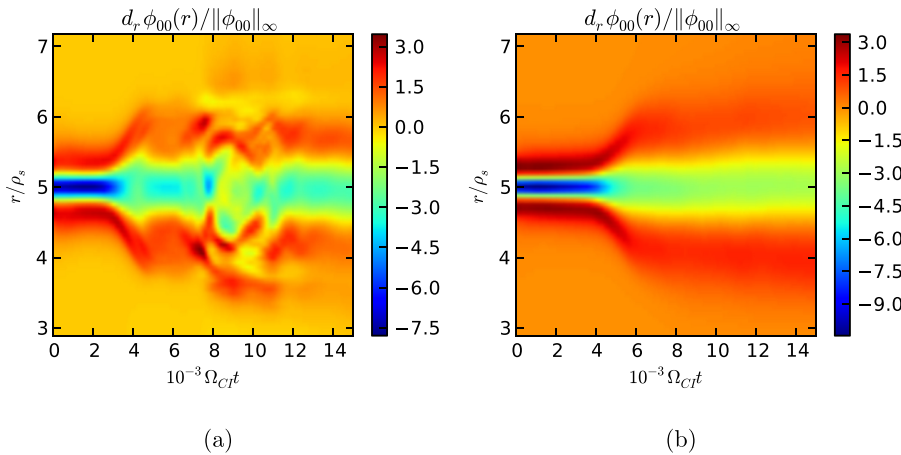


FIG. 18. SMALL case; time evolution of the normalized mean poloidal velocity for single mode perturbation by (10, 5) (a) and 239 modes perturbation (b).

In few modes perturbation cases, the first stages are dominated by the interplay of the few perturbed modes with the (0, 0) one, and spectral broadening becomes significant later (Fig. 19(a)). The initially broad and flat spectrum is first reshaped in the linear phase in accordance with the linear growth rates ordering; this does not lead to a strong spectral narrowing as the linear growth-rate variation is mild around the most unstable mode (Fig. 19(b)). Though as stated earlier no strict steady state is attained, observation of the evolution of the electrostatic potential  $k_\perp$  spectrum reveals a convergence towards a power-law tailed spectrum (Fig. 20). A more direct observation of the evolution of perturbation geometry can be done for 1-mode perturbations: Fig. 21 shows the perturbed ionic density at key instants of the simulation. Fig. 21(a) shows the initial mode structure which is preserved throughout the linear growth phase. Figs. 21(b)–21(e), taken after the first saturation of the (6, 3) mode, show the progressive poloidal shearing of the

convective cells and the birth of smaller convective structures. In Fig. 21(f), at the end of the simulation, the perpendicular structure is strongly dominated by the zonal flow.

### B. First saturation mechanism

Saturation of the instability occurs through two main mechanisms:

- the growth of the (0, 0)-mode, driven by the self-coupling terms of the Reynolds stress in Eq. (6), leads to generation of an azimuthal shear flow, or zonal flow, and relaxation of the mean gradients radial profiles.
- the harmonic cascades driven by the quadratic coupling terms of Eq. (3) transfer energy from the perturbed mode to the rest of the spectrum.

In the nonlinear simulations, both mechanisms operate, and the interplay between all modes prevents a clear

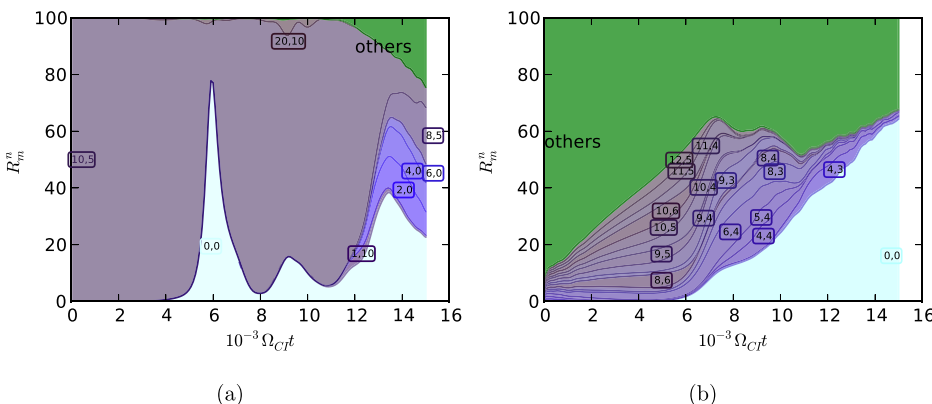


FIG. 19. SMALL case; filtered power spectra ratios  $R_m^n = \|\phi_m^n\|_2^2 / (\sum \|\phi_m^n\|_2^2)$ ; 1-mode perturbation by (10, 5) (a); bath of 239 modes (b)—modes for which  $\max R_m^n < 5\%$  are binned as “others.”

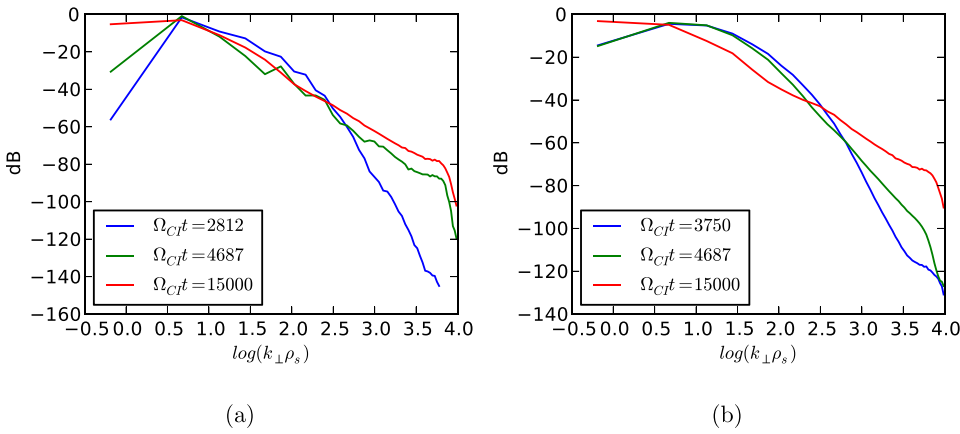


FIG. 20. SMALL case; electrostatic potential normalized power spectra; single mode perturbation by (10, 5) (a); 239 modes perturbation (b)

separation. In the quasi and linear models, no harmonics generation can occur, and saturation occurs only by the back reaction of the (0, 0) mode on unstable modes. In order to insure that the (0, 0) mode is the same in the nonlinear and quasilinear models, the later is used with the (0, 0) mode

imported from the nonlinear simulation: divergence of the two models can then be interpreted as a clear signature of the second saturation mechanism. In the case single mode perturbations simulations, the nonlinear and quasilinear models are in agreement up to the first saturation stage, while the linear models predicts a faster quenching of the unstable mode. (Fig. 22). Saturation can then be attributed exclusively to the effect of the zonal flow. Moreover, divergence of the linear model with the quasi and nonlinear ones can be attributed to the fast evolution of the (0, 0) flow just before saturation, which breaks the adiabaticity hypothesis.

Now linear instability quenching by the (0, 0) mode can itself be considered as a twofold mechanism: an unstable mode can be stabilized by relaxation of the mean gradients ( $k_{\theta} d_r v_{j0}^0$  term in Eq. (7)) which reach under-threshold levels or through the Doppler shift induced by the zonal flow shearing rate term  $k_{\theta} d_r \phi_0^0$  in Eq. (7). Estimating the relative weight of both mechanisms is simply done in the linear and quasilinear models by nullifying the shearing-rate term and checking for discrepancies. For the first saturation stage, the effect of the zonal flow shearing rate appears to be negligible, and the saturation is driven by the contour gradients evolution. For broad spectrum perturbations, the saturation mechanism is more intricate. The quasi and nonlinear models diverge, which implies a non-negligible influence of the (in that case numerous) nonlinear couplings other than with the (0, 0) mode (Fig. 23). Let us now consider two specific modes, differing by their initial growth rate. For the SMALL case, the mode (10, 5) is the most unstable in the whole ( $m, n$ ) plane for the initial equilibrium. As can be seen by comparing Figs. 22(b) and 23(b), the saturation processes are similar in the single perturbation and bath case, with first saturation durations of about  $2000\Omega_{CI}^{-1}$ . This can be expected since at the end of the linear phase, the Reynolds stress driving the zonal flow (through (6)) is dominated by the terms stemming from the most unstable modes, among which (10, 5) is the most unstable. For the (6, 3) mode (Figs. 22(a) and 23(a)), it can be noticed on the first hand that the first saturation process is slower for all models in the case of the mode bath perturbation, with a characteristic duration of about  $8000\Omega_{CI}$ . Considering the quasilinear evolution to exclude nonlinear couplings influence, it appears that the back-reaction of the zonal flow on the (6, 3) mode is more efficient when the zonal flow is generated exclusively by this mode.

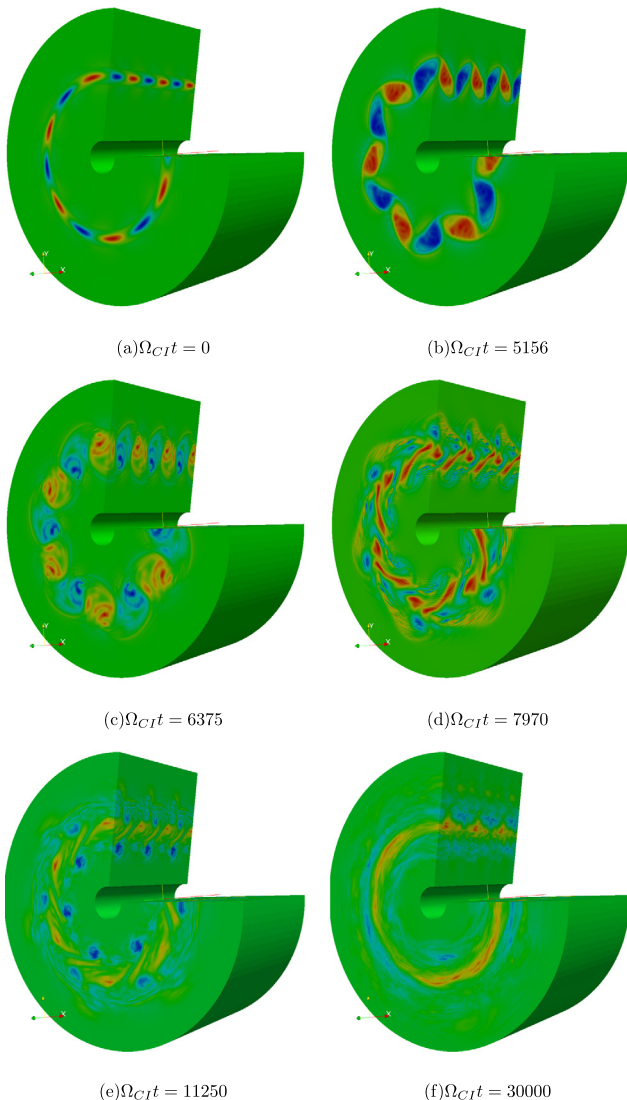


FIG. 21. SMALL case perturbed by (6, 3); snapshots of perturbed density  $n(\mathbf{r}, t) - n(\mathbf{r}, 0)$

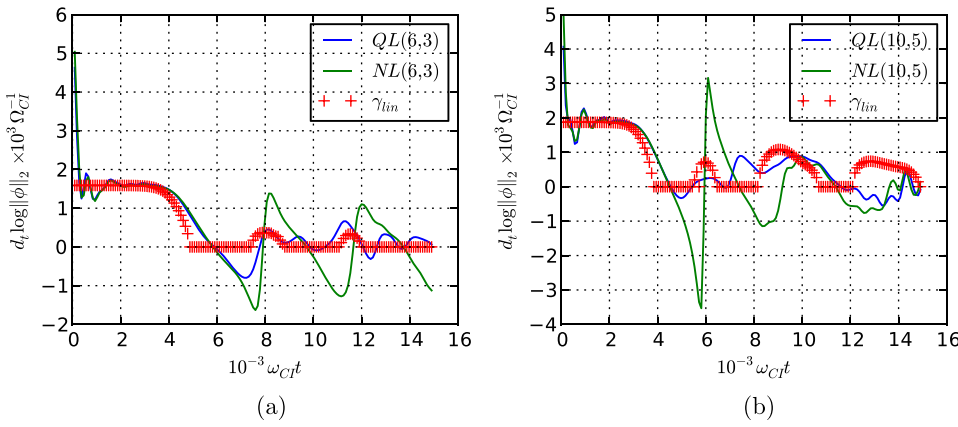


FIG. 22. SMALL case; comparison of pseudo growth rates of nonlinear and quasilinear potential Fourier modes with linear growth rate; single mode perturbation by (6, 3) (a) and (10, 5) (b).

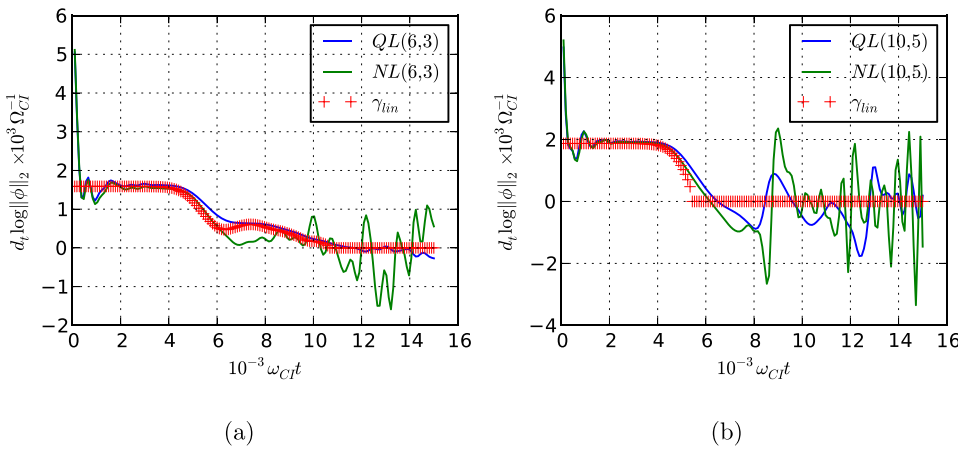


FIG. 23. SMALL case; comparison of pseudo growth rates of nonlinear and quasilinear potential Fourier modes with linear growth rate; perturbation by 239 modes; results for modes (6, 3) (a) and (10, 5) (b).

This phenomenon is also observed for the two-modes perturbation by (6, 3) and (10, 5): the mere fact that in that case the zonal flow is driven dominantly by (10, 5) breaks the correlation between (6, 3) and (0, 0) (Fig. 24). A remarkable fact can be noticed on in the 2-modes and bath perturbation case (Figs. 24(b) and 24(c)): the most unstable mode (10, 5), which drives the zonal flow is quenched first by (0, 0) mode back reaction, allowing the initially less unstable (6, 3) mode to grow and reach higher levels than the (10, 5) mode. Trying to evaluate naively turbulence  $(m, n)$  spectrum after the first saturation from spectral data computed at  $t=0$  would in that case be erroneous since the early quenching of the initially most unstable modes can lead to spectral ordering inversion: relaxation towards linear marginal stability is not a uniform process in the  $(m, n)$  spectral plane (Fig. 25)

On the second hand, the linear growth rate shows a surprisingly good agreement with the nonlinear one at the

beginning of the saturation (Fig. 23(a)) between  $t = 4000 \Omega_{CI}^{-1}$  and  $t = 6000 \Omega_{CI}^{-1}$ . This should not be interpreted as a success of the linear model, but an effect of the nonlinear couplings which happen to compensate for the model divergence. The good agreement of the linear and quasilinear model between  $t = 6000 \Omega_{CI}^{-1}$  and  $t = 10\,000 \Omega_{CI}^{-1}$  (Fig. 23(a)) is the sign that the adiabaticity condition is restored as the (0, 0) mode evolution slows down due to saturation of the most unstable modes (Fig. 23(b)).

### V. CLOSING REMARKS

Previous numerical experiments<sup>3</sup> showed good agreement of the three dynamical models examined in the linear growth phase of the instability. It is thus possible in this phase to describe accurately the system state, zonal flows included, using only linear normal modes. To that end, the knowledge

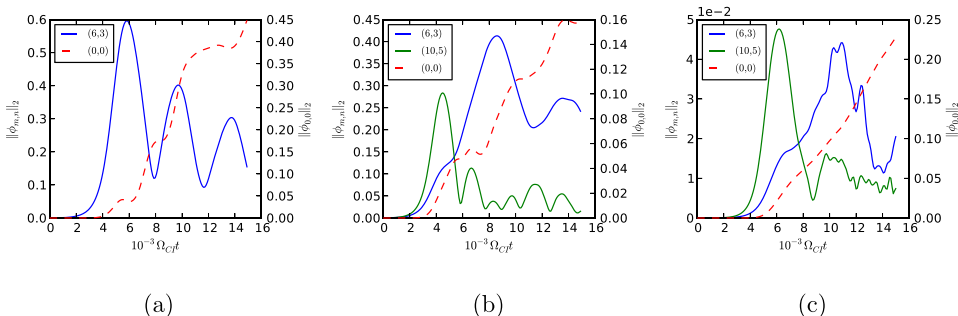


FIG. 24. SMALL case; radial  $L_2$  norm of electrostatic potential; (a) single mode perturbation by (6, 3); (b) two modes perturbation by (6, 3) and (10, 5); (c) 237 modes perturbation

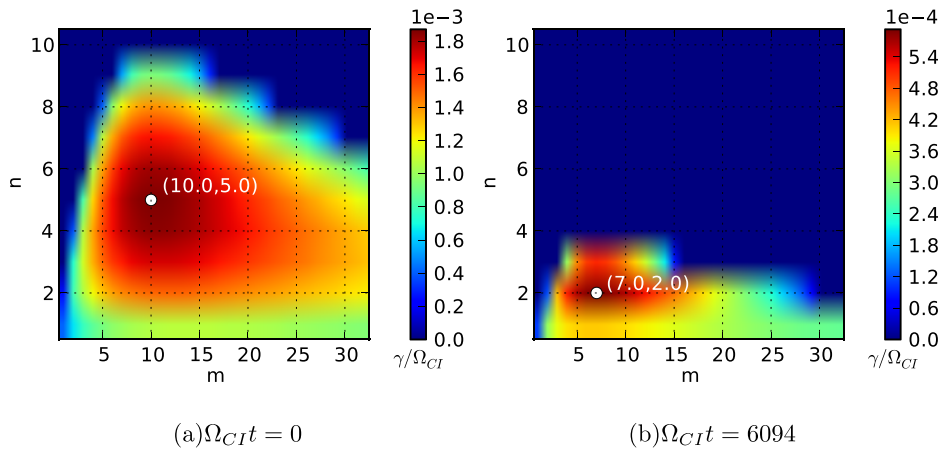


FIG. 25. SMALL case perturbed by 239 modes; linear growth rate map of initial equilibrium (a) and computed from nonlinear simulation mean fields at  $\Omega_{CI}t = 6094$  (b).

of both temporal and geometric characteristics of the dominant normal modes must be recovered, justifying the need to fully solve the linear eigenvalue problem. Moreover, the sampling artifacts (lobe structure) of the multi-water-bag model observed in previous local models<sup>14</sup> are less pronounced in the global one, at the price of a more constrained water-bag parameter setting procedure. Nonetheless, as the sensitivity of linear modes characteristics on parallel velocity sampling increases when one considers modes closer to marginal stability, some care must be taken to adapt the number of bags used to the required accuracy. Numerical results of linear, quasilinear, and nonlinear simulations presented here show that, apart from the obvious effect of nonlinear couplings, the linear description can fail to capture the dynamics of the system because of the fast relaxation of the mean fields during early saturation stages. Moreover, the non uniformity of the stabilization of linearly unstable modes in the  $(m, n)$  spectral plane by zonal flow evolution has a non negligible impact on the post-saturation spectrum.

<sup>1</sup>N. Besse and P. Bertrand, "Gyro-water-bag approach in nonlinear gyrokinetic turbulence," *J. Comput. Phys.* **228**, 3973–3995 (2009).

<sup>2</sup>A. J. Brizard and T. S. Hahm, "Foundations of nonlinear gyrokinetic theory," *Rev. Mod. Phys.* **79**, 421–468 (2007).

<sup>3</sup>D. Coulette and N. Besse, "Numerical comparisons of gyrokinetic multi-water-bag models," *J. Comput. Phys.* (to be published).

<sup>4</sup>B. D. Fried and S. D. Conte, *The Plasma Dispersion Function* (Academic Press, New York, NY, 1961).

<sup>5</sup>X. Garbet, Y. Idomura, L. Villard, and T. H. Watanabe, "Gyrokinetic simulations of turbulent transport," *Nucl. Fusion* **50**(4), 043002 (2010).

<sup>6</sup>V. Grandgirard, Y. Sarazin, X. Garbet, G. Dif-Pradalier, Ph. Ghendrih, N. Crouseilles, G. Latu, E. Sonnendrücker, N. Besse, and P. Bertrand, "Computing ITG turbulence with a full-f semi-lagrangian code," *Commun. Nonlinear Sci.* **13**(1), 81–87 (2008).

<sup>7</sup>E. Gravier, R. Klein, P. Morel, N. Besse, and P. Bertrand, "Gyrokinetic-water-bag modeling of low-frequency instabilities in a laboratory magnetized plasma column," *Phys. Plasmas* **15**(12), 122103 (2008).

<sup>8</sup>T. Görler, X. Lapillonne, S. Brunner, T. Dannert, F. Jenko, F. Merz, and D. Told, "The global version of the gyrokinetic turbulence code gene," *J. Comput. Phys.* **230**(18), 7053–7071 (2011).

<sup>9</sup>W. Horton, "Drift waves and transport," *Rev. Mod. Phys.* **71**, 735–778 (1999).

<sup>10</sup>K. Itoh, S.-I. Itoh, P. H. Diamond, T. S. Hahm, A. Fujisawa, G. R. Tynan, M. Yagi, and Y. Nagashima, "Physics of zonal flows," *Phys. Plasmas* **13**(5), 055502 (2006).

<sup>11</sup>S. Jolliet, A. Bottino, P. Angelino, R. Hatzky, T. M. Tran, B. F. Mcmillan, O. Sauter, K. Appert, Y. Idomura, and L. Villard, "A global collisionless pic code in magnetic coordinates," *Comput. Phys. Commun.* **177**(5), 409–425 (2007).

<sup>12</sup>R. Klein, E. Gravier, P. Morel, N. Besse, and P. Bertrand, "Gyrokinetic water-bag modeling of a plasma column: Magnetic moment distribution and finite larmor radius effects," *Phys. Plasmas* **16**(8), 082106 (2009).

<sup>13</sup>P. Morel, E. Gravier, N. Besse, A. Ghizzo, and P. Bertrand, "The water bag model and gyrokinetic applications," *Commun. Nonlinear Sci.* **13**, 11–17 (2008).

<sup>14</sup>P. Morel, E. Gravier, N. Besse, R. Klein, A. Ghizzo, P. Bertrand, X. Garbet, P. Ghendrih, V. Grandgirard, and Y. Sarazin, "Gyrokinetic modeling: A multi water bag approach," *Phys. Plasmas* **14**(11), 112109 (2007).

<sup>15</sup>P. H. Diamond, S.-I. Itoh, K. Itoh, and T. S. Hahm, "Zonal flows in plasma: A review," *Plasma Phys. Controlled Fusion* **47**(5), R35–R41 (2005).